THE ASTRONOMICAL JOURNAL VOLUME 108, NUMBER 4 OCTOBER 1994

EMBEDDED CLUSTERS IN GIANT EXTRAGALACTIC H II REGIONS. I. *BVR*Hα PHOTOMETRY

Y. D. MAYYA[1]

Indian Institute of Astrophysics, Bangalore 560 034, India
Electronic mail: ydm@tifrvax.tifr.res.in

Received 1994 December 30; revised 1994 May 16

ABSTRACT

Photometry in *BVR* continuum bands and in the emission line of Hα+[N II] are presented for a sample of H II complexes in disk, spiral arm and nuclear regions of galaxies NGC 1365, 1566, 2366, 2903, 2997, 3351, 4303, 4449, and 5253. Main sources of errors on H II region photometry are discussed. Errors due to background subtraction are parametrized in terms of background nonuniformity and fractional background contribution and are described separately in the Appendix. Our photometric data are compared with the existing data in the literature. Photometric properties of the sample regions are analyzed statistically and its implications on star formation are briefly discussed. Colors and Hα+[N II] equivalent widths of nuclear H II regions are found to be distinctly different from disk H II regions, suggesting different star formation histories. We have identified a few high Hα+[N II] equivalent width regions, which are fainter than average in both emission line and continuum fluxes, thus accounting for the low frequency of occurrence of such regions in flux limited samples.

1. INTRODUCTION

Giant Extragalactic H II Regions (GEHRs) are ionized regions embedding clusters of young and massive stars. They trace spiral arms in spiral galaxies and give a chaotic structure to irregulars. Compared to most familiar galactic H II regions, GEHRs are larger, brighter, less dense (O'Dell & Castaneda 1984a, b; Kennicutt 1984) and more turbulent (Melnick 1977; Roy *et al.* 1986; Hippelein 1986; see, also, Shields 1990 for a recent review of physical properties). Their high Balmer luminosities indicate that they harbor hundreds or thousands of solar mass in OB stars, emitting copious amounts of ionizing photons ($\log N_L$ ph s^{-1} =50–53) equivalent to tens or even thousands of O5 V stars (Kennicutt & Chu 1988). The embedded clusters are young as evidenced by the presence of short-lived O stars, and at present contain all the stars that are formed in the latest star formation event. Hence these regions are ideally suited for the study of star formation and stellar initial mass function (IMF) over a wide range of stellar masses. However 30 Doradus in the Large Magellanic Cloud is the only GEHR in which stellar population is studied by direct star count method, with fair degree of success (see, e.g., Parker & Garmany 1993). Wolf–Rayet stars, the evolved descendants of massive stars have been isolated in nearby galaxies such as NGC 595 and 604 in M33 (Drissen *et al.* 1993a), NGC 2363 in NGC 2366 (Drissen *et al.* 1993b) and several regions in NGC 300 (Schild & Testor 1992) mainly because of their characteristic He II λ4686 Å emission. Obviously star count methods cannot be used in farther galaxies, because of lack of resolution or faintness or both. Hence indirect methods based on integrated properties have to be adopted for the stellar population studies in GEHRs as a class. Hitherto such indirect studies have been mainly used to investigate the global star formation histories of galaxies (Huchra 1977; Larson & Tinsley 1978; Kennicutt 1983; Gallagher *et al.* 1984), for an assumed set of IMF parameters.

The main interest in H II regions over the years has been in the study of elemental abundances and their gradients in galaxies. A number of regions have been observed spectroscopically for this purpose (see Dinerstein 1990, and the references therein). One of the by-products of these spectroscopic observations is the Hβ equivalent widths. Availability of the Hβ equivalent widths for a large number of GEHRs has motivated several groups to use Hβ equivalent widths for a study of star formation and IMF parameters (see Scalo 1986). However this suffers from the following problem. Often the slits used in spectroscopy are small, sampling only the peaks in the Hβ distribution and hence the observed flux ratios such as Hβ equivalent widths may not be representative of the entire region. To overcome this problem we used CCD imaging data to obtain fluxes in Hα+[N II] and continuum bands. In the program galaxies the contribution of [N II] to the combined Hα+[N II] flux varies between 10%–30%, as computed from the available spectroscopic line ratios. The higher values correspond to low excitation regions, which are plenty in the present sample. However Hα emission dominates the flux obtained within the filter even for these low excitation regions and hence in the remaining part of the paper, the Hα+[N II] flux is simply referred to as Hα flux, with remarks made when appropriate. Background subtracted fluxes over the entire extent of H II regions were obtained accurately through synthetic aperture photometry on CCD images. This process reduces the uncertainties due to the insufficient slit sizes.

The present work is aimed at providing uniform photometric data on individual GEHRs which can be used for the investigation of star formation properties. In this paper, we present photometric results on a total of 186 regions in galaxies NGC 1365, 1566, 2366, 2903, 2997, 3351, 4303, 4449, and 5253. Observational and reduction details employed in

[1]Present address: Infra Red Astronomy Group, Tata Institute of Fundamental Research, Homi Bhabha Road, Colaba Bombay 400 005, India.

 0004-6256/94/108(4)/1276/16/$0.90

TABLE 1. Sample of galaxies.

Galaxy NGC	deV. Type	A_v(gal)	Incl. (°)	Velocity km s^{-1}	Distance (Mpc)	Reference dist	Reference spect	N(H II)	Region
1365	SB(s)b	0.159	56	1502	10.0	1	10,11	5	NW arm
1566	SAB(s)bc	0.212	36	1178	13.0	2	12,13	5	NW arm
2366	SBm	0.303	62	252	3.6	3	14,15	1	NGC 2363
2903	SAB(rs)bc	0.166	58	467	10.0	4	16	8	N+S
2997	S(s)c	0.408	37	805	10.0	5	17,18	49	NE+SW arm
3351	SB(r)b	0.144	46	673	8.5	6	16	4	Centre
4303	SAB(rs)bc	0.151	24	1483	19.0	7	19	10	Centre
4449	IBm	0.151	44	262	5.0	8	16,20	3	Centre
5253	Irr IIp	0.144	64	209	2.0	9	21	1	Nucleus

Notes to TABLE 1

(1) Jones and Jones (1980)
(2) Pence, Taylor and Atherton (1990)
(3) Sandage and Tammann (1976)
(4) Sandage and Tammann (1981)
(5) Peterson (1978)
(6) Bottinelli *et al.* (1984)
(7) Kennicutt (1981)
(8) Sandage and Tammann (1975)
(9) de Vaucouleurs (1979)
(10) Roy and Walsh (1988)
(11) Alloin *et al.* (1981)
(12) Roy and Walsh (1986)
(13) Hawley and Phillips (1980)
(14) Peimbert, Peña, and Torres-Peimbert (1986)
(15) Kennicutt, Balick and Heckman (1980)
(16) McCall, Rybsky and Shields (1985)
(17) Walsh and Roy (1989b)
(18) Roy and Walsh (1987)
(19) Shields, Skillman and Kennicutt (1991)
(20) Lequeux *et al.* (1979)
(21) Walsh and Roy (1989a)

obtaining calibrated BVR and Hα+[N II] photometry are described in Secs. 2 and 3. Section 4 contains the photometric results and identification charts. Photometric properties of disk H II regions are compared with nuclear H II regions in Sec. 5. In Paper II of this series we will describe a population synthesis model, synthesizing the observational quantities. The results of comparing the observations with the models will be presented in Paper III.

2. THE SAMPLE, OBSERVATIONS AND REDUCTIONS

The observations were aimed at obtaining uniform photometric data in BVRHα bands for a sample of GEHRs in nearby galaxies. The chosen galaxies have published spectroscopic data on at least a few GEHRs in them. Table 1 lists the sample of galaxies. The number of regions for which good spectroscopic data are available in the literature is given in the table along with relevant references. Because of the large angular sizes of the galaxies compared to the CCD size (137×207 arcsec^2) only selected regions in the galaxies could be observed. The regions selected are given in the last column in the table. The estimated galactic visual extinction to the galaxy (de Vaucouleurs *et al.* 1976) is also given in the table.

Hα+[N II] emission line and BVR broadband photometry of the sample galaxies were carried out with the help of CCD imaging using the 1 m telescope at Vainu Bappu Observatory (VBO), Kavalur. The CCD system used is from Photometrics Ltd., Arizona, and uses a Thomson-CSF CCD chip, coated for enhanced ultraviolet sensitivity. At the Cassegrain focus, the pixel size of 23 μm corresponds to an image scale of 0.36 arcsec pixel^{-1}. All the observations were carried out during 1990–92 observing seasons. Schott glass combinations as recommended by Bessell (1990) were used as BVR filters, while an interference filter of bandwidth 160 Å is used as Hα filter, during 1990–1991 observations. 1992 observations were carried out using coated filters, which were calibrated using similar methods as for the previous set. While the earlier set of filters closely matched the standard set, color coefficients for the latter set suggested that the V and R bands are close to the standard Cousins while the effective wavelength of B band is shifted towards the red side. See Mayya (1991, 1993) for the calibration details of the filters and CCD system. The 160 Å Hα filter had almost square passband with the measured efficiency of the Hα filter within 85% of the peak even for galaxies with highest recessional velocities in the sample. Scaled R band fluxes were used to estimate the in-band continuum in Hα filter. Spectrophotometric and photometric standard stars were used to obtain the scaling factor between the R band and Hα filter. The dependence of the scaling factor was found to be negligible with color for the normal range of colors of H II regions and galaxies as discussed in detail in Mayya (1991). In subtracting the continuum, we followed equations described in Waller (1990). Thus the small contamination of R band due to Hα has been taken into account during the continuum subtraction. The scaling and continuum subtraction are done on the measured aperture magnitudes rather than on the image itself, so as to reduce processing errors (Newberry 1991). However the quoted R magnitudes, like B and V are observed values and hence include emission contribution from the surrounding nebula. Subtraction of nebular contribution in broadbands requires the knowledge of physical conditions in the ionized gas as illustrated by Huchra (1977). We will come back to this topic again in Paper III, while obtaining pure BVR magnitudes of embedded clusters.

Generally Hα images were of 30 min duration and the exposure time for BVR ranged from 10–30 min. Typically 2–3 frames were acquired for every field in all the filters. Point spread function measurements were done by fitting the profiles on the stars within the galaxy frames and lie in the range 1.5–3.5 arcsec. For two of the galaxies (NGC 2903 and 2997) we had two settings so as to cover the main optical disks. Only north–west part could be observed in NGC 1365. For the remaining galaxies, observations were done keeping the nucleus at the center of the CCD. The longer axis of the CCD was maintained along east–west within the errors of few degrees ($\leq$5°) on all nights in 1991–92. The angle was more than 5° on some of the nights in 1990. All observations were done with the default gain (cgain=0 or 27.7 electron count^{-1}) in 1991 and earlier and with cgain=33 [13.7 electron count^{-1}, Prabhu *et al.* (1991)] in 1992. For one of the galaxies in the sample (NGC 2366), Hα frame is obtained using the CCD system at the 2.34 m Vainu Bappu Telescope in 1990 (see Bhat *et al.* 1992 for calibration).

As this was the first attempt in carrying out photometry of nonstellar objects like H II regions with the CCD systems at the observatory, much attention was given to calibration. For the southern galaxies in the sample, $UBVRI$ photometric standard stars drawn from the list of Hamuy & Maza (1989) were observed, whenever the sky appeared photometric. The methods followed in using the frames from nonphotometric nights are discussed in Sec. *4.2*. Extinction coefficients were determined on all photometric nights. Spectrophotometric standard star EG 99 (Oke 1974), which is also a $UBVRI$ photometric standard (Kilkenny & Menzies 1989), was observed on almost every photometric night. Another standard

TABLE 2. Surface brightness of H II regions and background.

NGC	V(H II)	μ_V(H II)	μ_V(bkg+sky)	γ_V	ΔV	$\Delta(B-V)$	N
1365	17.24±1.11	21.98±0.69	20.86±0.48	0.73±0.08	0.43±0.33	−0.16±0.17	13
1365[1]	14.84±0.44	18.71±0.60	19.30±0.70	0.38±0.16	0.08±0.05	0.02±0.04	3
1566	16.71±0.97	21.35±0.58	19.51±0.14	0.83±0.09	1.01±0.76	0.03±0.97	12
2903	18.05±1.45	22.22±1.40	20.11±0.28	0.84±0.08	0.77±0.37	−0.20±0.26	12
2903[1]	15.11±0.43	18.44±0.34	18.85±0.18	0.41±0.08	0.08±0.03	−0.01±0.01	6
2997[2]	18.89±0.82	22.43±0.85	20.13±0.06	0.87±0.08	1.17±1.33	−0.33±1.38	36
2997[3]	17.14±0.78	22.52±0.53	20.13±0.07	0.89±0.05	1.14±0.54	−0.18±0.79	9
2997[4]	17.91±0.90	22.20±0.51	19.99±0.02	0.88±0.05	1.20±0.64	−0.18±0.47	15
3351[1]	14.96±0.54	18.28±0.30	19.36±0.19	0.27±0.05	0.04±0.01	−0.01±0.01	6
4303	18.10±1.20	21.88±1.05	20.05±0.17	0.81±0.10	0.81±0.58	−0.23±0.51	40
4303[3]	16.21±0.66	21.49±0.83	20.17±0.15	0.74±0.14	0.58±0.45	−0.07 ± 0.68	16

NGC	$F\alpha$(H II)	μ_α(H II)	μ^1_α(bkg+sky)	γ_α	$\Delta F\alpha$	$\Delta(V-R)$	N
1365	−12.90 ± 0.25	−14.71 ± 0.29	−14.57 ± 0.18	0.58 ± 0.08	−0.07±0.03	−0.44±0.40	13
1365[1]	−12.32±0.10	−13.90 ± 0.26	−13.91 ± 0.37	0.30 ± 0.13	−0.02 ± 0.01	0.01 ± 0.02	3
1566	−13.00±0.66	−14.87 ± 0.61	−14.12 ± 0.08	0.68 ± 0.21	−0.21 ± 0.18	−0.00 ± 0.58	12
2903	−13.00±0.32	−14.68 ± 0.25	−14.30 ± 0.13	0.63 ± 0.10	−0.10 ± 0.06	−0.02 ± 0.39	12
2903[1]	−13.08±0.84	−14.42 ± 0.89	−13.80 ± 0.07	0.37 ± 0.11	−0.03 ± 0.02	−0.00 ± 0.02	6
2997[2]	−13.68±0.32	−15.09 ± 0.31	−14.39 ± 0.05	0.70 ± 0.12	−0.16 ± 0.13	0.05 ± 1.25	36
2997[3]	−12.98±0.32	−14.13 ± 0.24	−14.40 ± 0.05	0.74 ± 0.11	−0.22 ± 0.18	−0.64 ± 1.42	9
2997[4]	−13.37±0.36	−15.09 ± 0.31	−13.99 ± 0.02	0.88 ± 0.05	−0.41 ± 0.19	0.26 ± 0.46	15
3351[1]	−13.19±0.81	−14.52 ± 0.62	−14.10 ± 0.07	0.25 ± 0.04	−0.02 ± 0.00	−0.00 ± 0.00	6
4303	−13.43±0.40	−14.95 ± 0.41	−14.49 ± 0.07	0.64 ± 0.12	−0.11 ± 0.09	−0.12 ± 0.51	40
4303[3]	−12.89±0.35	−15.01 ± 0.33	−14.55 ± 0.05	0.64 ± 0.12	−0.15 ± 0.13	−0.12 ± 0.70	16

Notes to TABLE 2
[1] Nuclear H II regions or hotspots [2] North-east arm of NGC 2997
[3] Measurements with bigger apertures [4] South-west arm of NGC 2997
[†] Sky + background surface brightness within 160 Å filter centered around 6563 Å.

field which was routinely observed is the dipper asterism in M67 (Schild 1983). These observations help us to check the emission line calibration and scaling factors between the narrowbands and broadbands in addition to providing the broadband calibration.

Bias frames were taken at regular intervals of two hours during all observations. Pixel-to-pixel variations of bias value is found to be negligible and hence average value for a frame was taken as typical. Bias values were found to gradually decrease over a night (Mayya 1991), and hence the average value of the bias frame immediately following the object frame was used for bias subtraction. Flatfield frames exposed to the twilight skies were stacked and used for flat fielding the object frames. After these primary reductions the images of a particular field (a galaxy or a part of it) were brought into a common coordinate system. This was done using the routines XYFIT, RESAMPLE, etc. in the EDRS subpackage of STARLINK. The process involved can be summarized as follows. The common stars in frames to be aligned were identified first. Taking one of the frames as reference the coefficients for transforming other frames were computed using XYFIT, allowing a shift of the centers and rotation. The resultant coefficients were applied to the frame to be aligned using RESAMPLE, interpolating linearly between pixels, when necessary. The coefficients suggested negligible rotational term in most cases. It was possible to obtain more than three stars for alignment in all cases except NGC 2903 and NGC 3351. For these galaxies carefully selected H II knots were taken as references. Rms alignment errors were less than 0.5 pixel for majority of frames, with the errors not exceeding a pixel even in extreme cases. The magnitude measurements of H II regions on the aligned frames were done using aperture photometry, which is the topic of discussion of the next section.

3. H II REGION PHOTOMETRY

In the Appendix we discuss the methods and major problems encountered in H II region photometry. Regions for photometry were selected based on their brightness on Hα images. Some fainter regions were included if they were found to have very strong optical continuum. The aperture center and radius were chosen interactively on a color composite image formed by the superimposition of Hα, B and V band images, displayed on COMTAL display unit. It was noticed that the centers of H II regions in Hα frames do not always coincide with the continuum images, which necessitated the usage of both line and continuum images for chosing the center and radius. We believe each chosen region to be an independent GEHR. While chosing the radius, care is taken to enclose most of the emission from a region, minimizing the contamination from a neighboring region. Rectangular regions for sky+background measurements were chosen interactively around each H II region and an average value (count per pixel) was taken to represent sky +background for that region. Once the center and radius of apertures for H II regions and positions for background measurements were decided, these parameters were used for flux measurements on all the aligned frames. This procedure en-

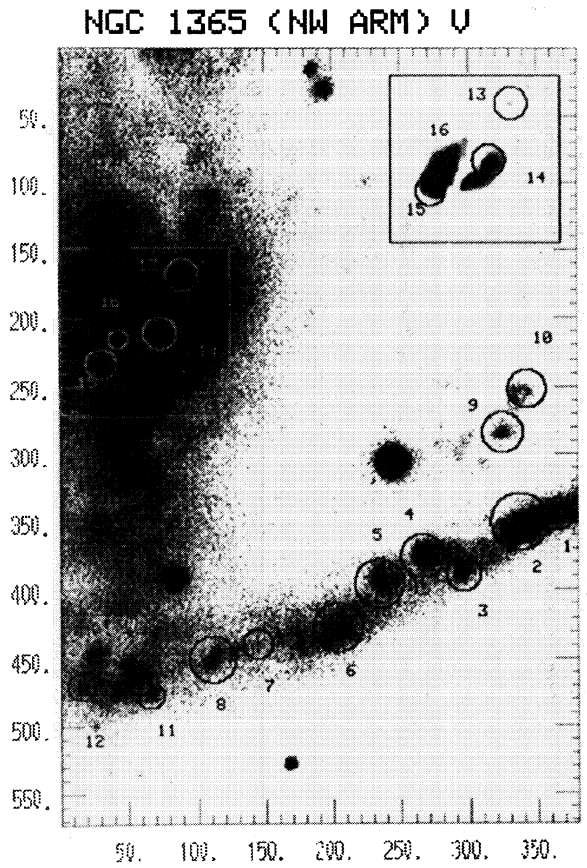

FIG. 1. A greyscale map of NGC 1365, identifying the regions selected for photometry. Circular apertures denote the area used for flux measurements. Axes are in pixel coordinates. North is to the right and east is to the top. Inset shows nuclear H II region with a different greyscale.

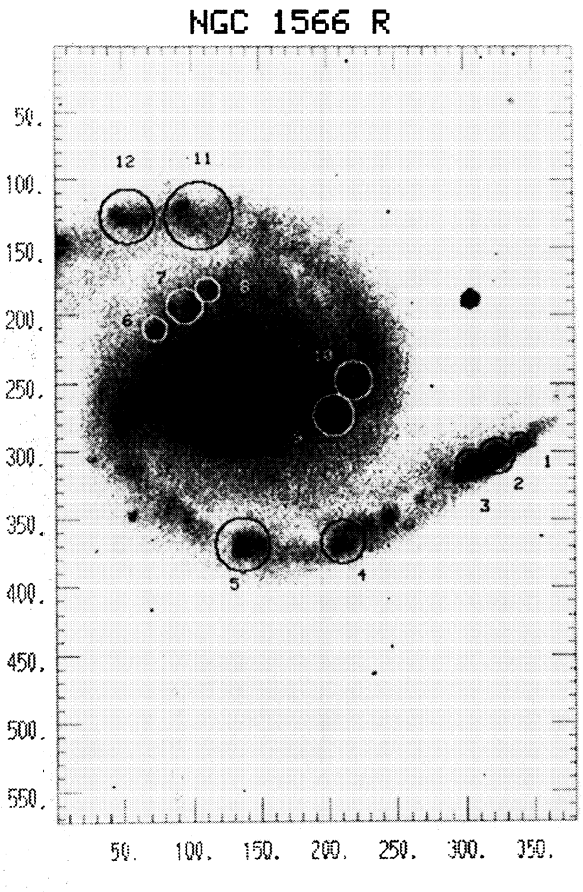

FIG. 2. NGC 1566. Details are similar to Fig. 1.

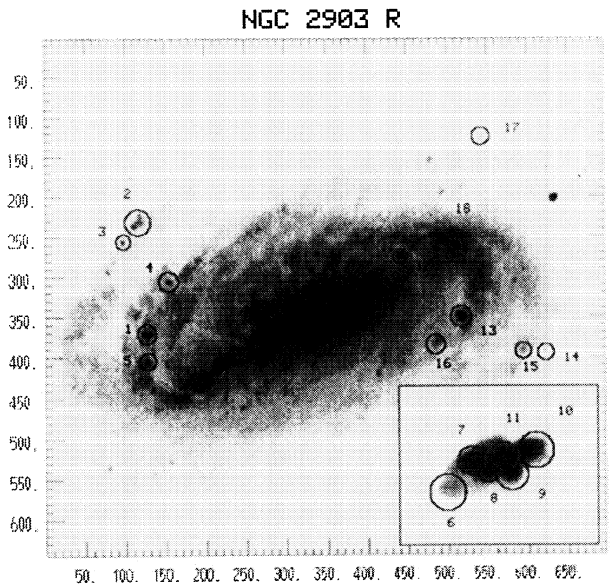

FIG. 3. NGC 2903. Details are similar to Fig. 1. The map is obtained by mosaicing two CCD images. The inset showing the nuclear H II regions is magnified by a factor of 2.5.

sures that fluxes measured on different frames using different filters correspond to the same region in the galaxy. Measurements were also done using bigger apertures enclosing more than one GEHR in galaxies NGC 2366, 2997, and 4303. These apertures often contain diffuse emission and possibly represent star forming complexes over kpc scale. We refer these regions as GEHR (Groups).

Some of the statistical properties relating to flux and surface brightness for the H II regions in the sample are listed in Table 2. Column 1 contains the NGC numbers of galaxies. Mean values are separately given for disk regions with small and large apertures and nuclear H II regions. The mean V band magnitude and surface brightness of H II regions along with the rms scatter are given in columns 2 and 3. Mean surface brightness was computed for each region by dividing the flux by the area of the H II region in arcsec^2. Mean sky +background surface brightness and the rms error on that are given in column 4. Column 5 contains the mean fractional contributions of the assumed sky+background within the aperture. The above quantities in Hα filter are given in log units in the bottom half of the table. Surface brightness in V and Hα bands are expressed in magnitude arcsec^{-2} and erg s^{-1} cm^{-2} arcsec^{-2}, respectively. The surface brightness of the sky+background within Hα filter is predominantly due to the red continuum. The amount by which the magnitudes and fluxes of H II regions might have been overestimated because of possible underestimation of background are given in column 6 (see the Appendix). This is computed using Eqn. (7) of the Appendix, assuming a background 10% higher than the measured value ($x=1.1$). The resultant errors on $B-V$ and $V-R$ colors are listed in column 7. Number of H II regions used for the above statistical analyses in each of the galaxies are given in the last column. This table is useful in assessing the errors on the derived magnitudes and colors due to the uncertainties in the background following the discussions in the Appendix.

4. PHOTOMETRIC CATALOGUE OF H II REGIONS

4.1 Identification Charts

Greyscale maps of program galaxies are produced from our images and are presented as Figs. 1–8. H II regions are identified by numbers with circles corresponding to the sizes of the apertures used. Numbers used during the identification on the display monitor are retained and no attempt is made to rearrange them according to any coordinate system. R band images are preferred in producing the maps as they contain contributions from both emission line and continuum. North is to the right and east is at the top of these maps. Numbers appearing on the grids are in pixel units (1 pixel=0.36 arcsec except for NGC 4449). Identifications of the nuclear H II regions in three Sersic–Pastoriza nuclei, NGC 1365, 2903, and 3351 (Sersic & Pastoriza 1965) are done separately on a different greyscale. Magnifications of 2.5 and 3 are used in the insets for NGC 2903 and 3351, respectively. Measurements with bigger apertures in galaxies NGC 2997 and 4303 are identified separately. The chart for NGC 2903 is produced as a mosaic of two images. A Prime Focus image using 2.34 m Vainu Bappu Telescope is used to produce the identification chart for NGC 4449. The scale for this image is

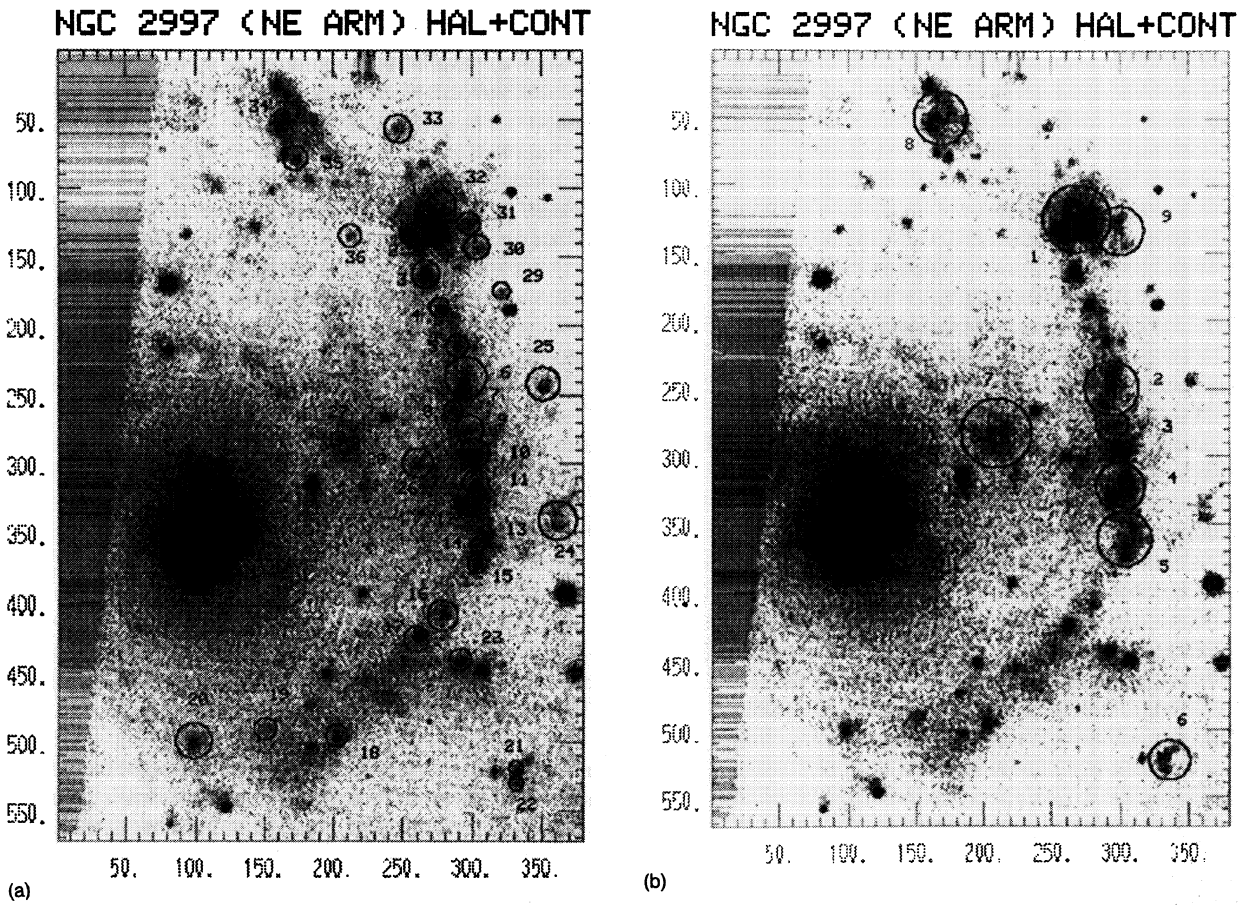

FIG. 4. NGC 2997-NE. Details are similar to Fig. 1. Magnitude measurements are also done using bigger apertures which enclose more than one emitting knot. In (a) smaller apertures are shown, whereas in (b) bigger apertures are shown.

1 pixel=0.56 arcsec and hence covers a larger field than the 1 m images. However only those regions covered by the 1 m telescope are selected for photometry.

4.2 The Catalogue

The calibrated photometric data on selected H II regions are presented in this section. Table 3 (this table is presented in its complete form in the ApJ/AJ CD-ROM Series, Vol. 3, 1994.) contains the results of our BVRHα+[N II] photometry. The descriptions of the items in the table are as follows.

(1) ID:H II region numbers as identified on the accompanying charts (Figs. 1–8).

(2)–(3) X, Y: The X and Y pixel coordinates on the aligned CCD images, which are the same as that appearing on the grid around identification charts. For NGC 4449 the grids contain different pixel numbers than that given in these columns for the reasons mentioned in the previous subsection.

(4)–(5) RA, DEC: Approximate position of the H II region, along right ascension and declination in seconds of arc, with respect to the galactic nucleus. These were obtained by transforming X and Y assuming that the RA–DEC axis is aligned with X–Y axis of the CCD. Since the alignment during observations is only approximate ($\leq 5°$), RA and DEC values away from the center are less accurate, compared to those near the center of the CCD. Thus the positions should be used only for identification purposes. E, W, N, and S preceding the numbers indicate, respectively, whether the H II region is to the east, west, north or south of the nucleus of the galaxy.

(6) DIA: Diameter of the aperture chosen for magnitude extractions in seconds of arc.

(7)–(9) V, $B-V$, $V-R$: V Magnitude, $B-V$ and $V-R$ colors of H II regions after subtracting assumed background. The rms errors on the measured magnitudes are in the range 0.05–0.10, as estimated from measurements on multiple frames.

(10) $\log F\alpha$: Logarithm of the observed Hα+[N II] flux in units of erg s^{-1} cm^{-2}. The values are accurate to 0.1 dex.

(11) W(Hα): Hα+[N II] emission equivalent width in Å with R magnitude as an estimate for the continuum at Hα. The following equation is used in the computations.

$$W(\mathrm{H}\alpha)(\text{Å}) = \frac{F_\alpha}{10^{-0.4(R+48.6+\kappa_r)}}\left(\frac{\lambda^2}{c}\right)$$
$$= \frac{F_\alpha(\mathrm{erg\ s^{-1}\ cm^{-2}})\times 1.633\times 10^{-11}}{10^{-0.4(R+48.6)}},$$

where λ and κ_r are the effective wavelength and zeropoint for R band (Bessell 1990). The measurement errors are ≤ 20

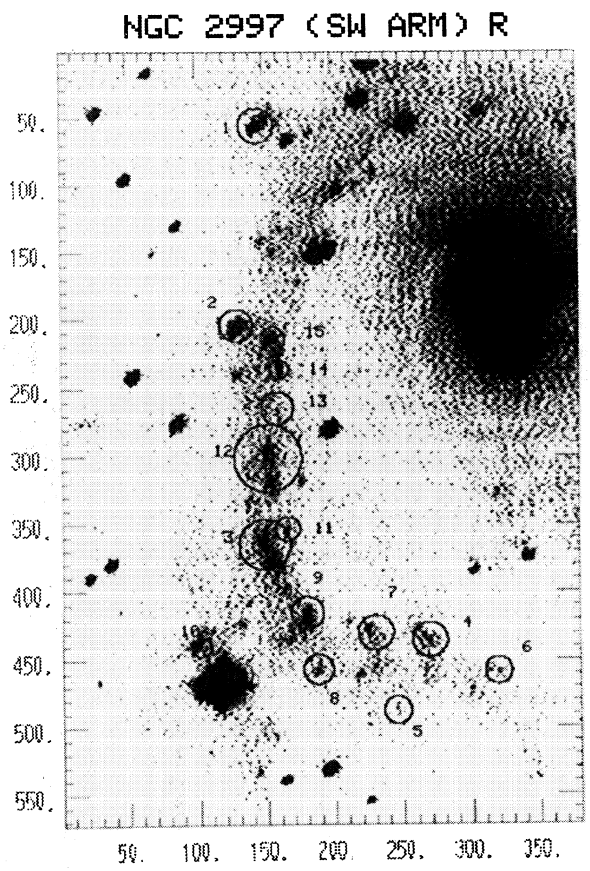

FIG. 5. NGC 2997-SW. Details are similar to Fig. 1.

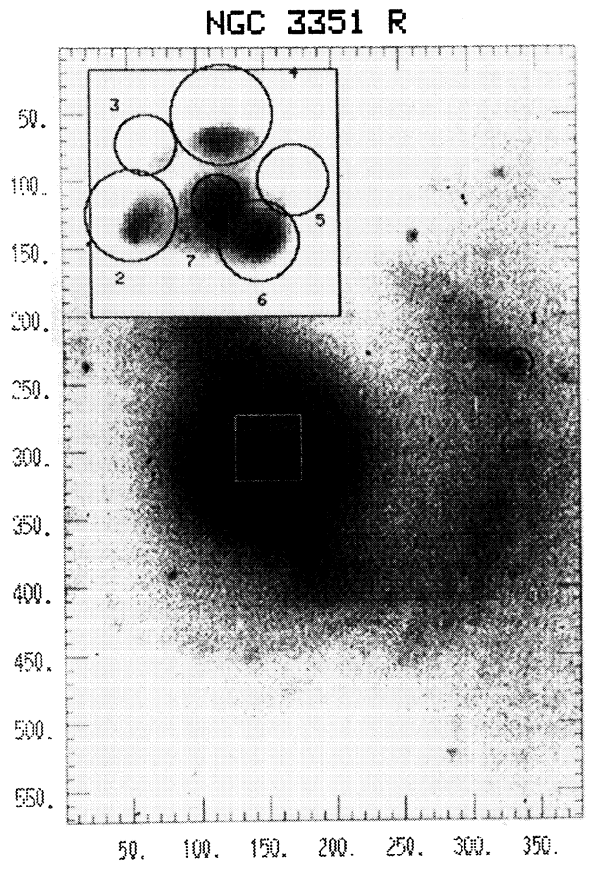

FIG. 6. NGC 3351. Details are similar to Fig. 1. The inset showing the nuclear H II regions is magnified by a factor 3.

Å. R band magnitudes used in the above definition include emission from the nebular continuum and lines.

(12) Qual.: An index of photometric quality. See the discussion below for definition.

(13) Other Id.: Identification from other authors when available. Notes to the table, list relevant references. For measurements with bigger apertures, individual GEHRs enclosed within the aperture are indicated.

The values in the catalogue are given a photometric quality index based on the errors on the derived $B-V$ and $V-R$ colors due to the uncertainty in the background estimation, following the methods discussed in the Appendix. Errors on BVR magnitudes are computed using Eq. (7) of the Appendix assuming $x=1.1$. The photometric quality is 1 if the computed errors on $B-V$ and $V-R$ is ≤ 0.1 mag. Similarly regions having errors between 0.1–0.2 are given an index 2, those between 0.2–0.3 are given an index 3. Index 4 means that the estimated errors in one of the colors is greater than 0.3 mag. It should be noted that the photometric quality index is only a measure of the background domination and is not actual error on colors. The higher the index, the more sensitive are the colors to the background measurement. As can be seen from Table 2 (column 7), correction for this uncertainty has the effect of making the colors systematically bluer than the catalogue values. The actual errors on the colors and magnitudes are less than this because a part the underestimated backgrounds might well be compensated by weak emissions from the extended halos outside the chosen apertures.

The rms errors on the measured magnitudes were estimated based on measurements on multiple frames as described below. First, the instrumental magnitudes were measured on all the available frames. Out of these measurements, the ones with the best photometric quality (or reference frame) are selected in each filter. Mean zero point shifts for the frames taken under nonideal photometric conditions were evaluated by comparing the measurements with that in the reference frame. These zero point shifts were applied on all the frames to bring all of them to the system of reference frame. Shifted magnitudes were combined with the reference magnitudes to obtain the mean magnitude and rms errors on these magnitudes. Typical errors are in the range 0.05–0.10 mag. Since $B-V$ and $V-R$ colors were obtained by independent BVR measurements, the errors on colors will be slightly larger. We estimate the final errors on the colors to be less than 0.15 mag.

The observed $B-V$ and $V-R$ colors are plotted against V magnitudes and Hα+[N II] equivalent widths in Fig. 9. The former set of plots is useful in checking any systematic dependence of colors on the magnitudes while the latter is useful in assessing the contamination of nebular emission on

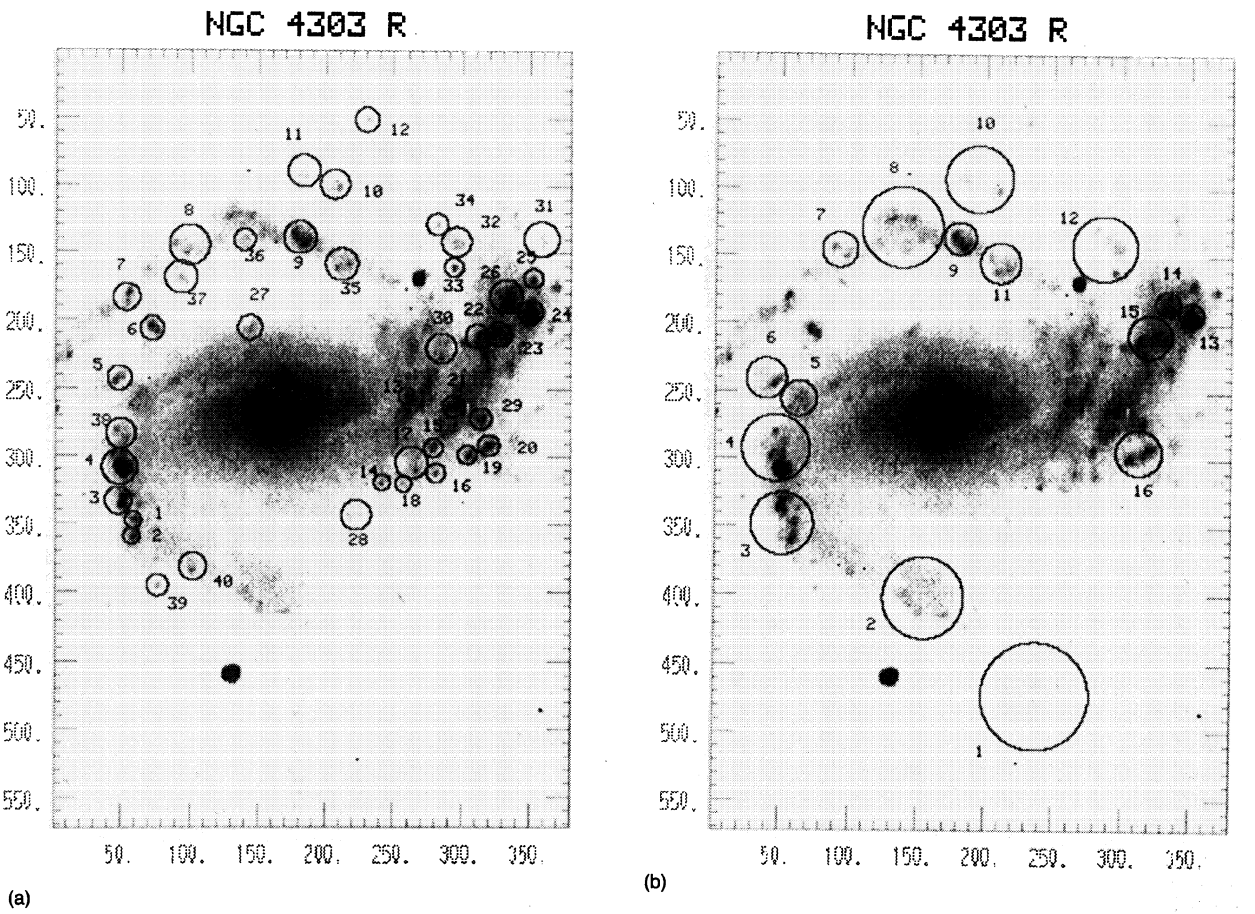

FIG. 7. NGC 4303. Details are similar to Figs. 1 and 4.

colors. Larger scatter in colors for fainter V magnitudes may be the result of increasing contribution of background. $V-R$ colors are expected to become redder with increasing Hα equivalent widths if gaseous emission contributes significantly. A slope of ~0.1 mag/100 Å Hα equivalent width is expected from Hα line contamination alone in R band. A trend of this order is clearly seen in galaxies NGC 2997 and 4303. $B-V$ colors do not show such trend. It may be noted that there are some GEHRs whose colors match or even exceed the disk colors, which lie in the range 0.4–0.8 in $B-V$ and 0.5–0.7 in $V-R$ for the galaxies studied here.

4.3 Comparison with Earlier Photometry

H II region photometry in BVR bands is rarely available in the literature. Hence the compilations of multiaperture photoelectric photometry around the nuclei of galaxies by Longo & de Vaucouleurs (1983) were used to check the zero points of our BV photometry. NASA Extragalactic Database[2] is also broused through for more recent photometry in BVR bands. Growth profiles were constructed around the nucleus of the program galaxies to compare with published photometry. Magnitudes with apertures greater than 10″ in the program galaxies were compiled from the literature and V magnitude differences are plotted against B magnitude differences in Fig. 10. When available R band differences are also plotted (filled circles). Aperture magnitudes in galaxies NGC 1365, 1566, 2903, 2997, 3351, 4303, and 4449 are plotted in Fig. 10(a), where as Fig. 10(b) contains measurements on NGC 5253 alone. Among the program galaxies this galaxy has the maximum number of earlier measurements. Errors on B and V magnitudes are of the same order and lie on either side of our measurements within 0.15 mag for all galaxies except NGC 5253. In NGC 5253 V magnitudes from different authors have larger spread than B magnitude. This may be due to the presence of strong [O III] λ5007 emission line at the tail of the V band response curve. Small differences in filter response of different observers would affect the photometry in the presence of emission rich spectrum of NGC 5253. As a whole it is clear from these figures that our photometry lies close to the centroid of measurements of different groups.

Unlike BVR photometry, Hα photometry of H II regions is extensively available in the literature, which is used to check our Hα calibration. We used the Hα photometry of Kennicutt (1988) and Hunter (1982) for comparison in galaxies NGC 2366, 4303, 4449, and 5253. Except in a few cases, aperture sizes were matched for comparisons. Another source of photometry is due to Roy and Walsh (see Table 1

[2]The NASA/IPAC Extragalactic Database (NED) is operated by the Jet Propulsion Laboratory, California Institute of Technology, under contract with the National Aeronautics and Space Administration.

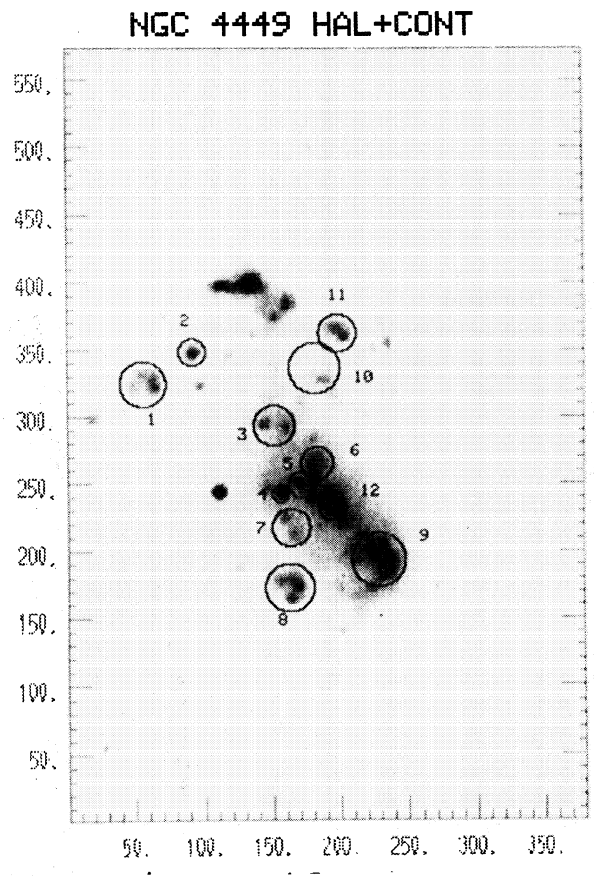

FIG. 8. NGC 4449. Details are similar to Fig. 1. This has a different image scale than the rest of the images.

for references). Using their Hβ fluxes and spectroscopic line ratios we computed the Hα+[N II] fluxes within their apertures. These fluxes were extracted in rectangular apertures and hence sampled areas cannot be matched with circular apertures. Areas covered by these authors exceed ours in most cases. Thus Roy and Walsh fluxes are compared after dividing by the corresponding areas. The resulting flux differences are plotted against our Hα fluxes in Fig. 11. The fluxes agree to within 0.1 dex for brighter regions with good matching of apertures. Two regions common to Kennicutt's sample, which have the largest discrepancies are NGC 4303 −9(HK 49) and NGC4303−G4(HK 155). The aperture mismatch is maximum in the former case, while the latter occurs in a crowded region, thus accounting for the observed discrepancies. The scatter increases at fainter ends with the fluxes of the faintest regions being systematically lower in our photometry. This difference might be arising due to one or more of the following reasons. At the fainter end, the regions are from Roy and Walsh sample, which on an average are fainter than those in the samples of Kennicutt and Hunter. The H II regions situated in the spiral arms cause additional problems because of the closeness of a neighbor. We may be missing the fainter extensions around H II regions because of nonregistration of images at very low count levels. However there may be some uncertainty in comparisons, because of totally different observing and reduction techniques followed. Thus we conclude that our Hα photometry is in general agreement with previous photometry for regions brighter than 10^{-13} erg s^{-1} cm^{-2}. At fainter levels our fluxes may be underestimated by factors 2–3, subject to the uncertainties in the comparisons. It should be noted that although the above comparisons indicate errors little larger than what is possible with the present day techniques, the systematic manner in which the photometry is performed makes the present data useful for statistical analysis. To our best knowledge, this is the first measurement of BVR magnitudes of GEHRs by CCD photometry.

5. COMMENTS ON GEHRs AND NUCLEAR H II REGIONS

H II regions catalogued by us are grouped into three categories. Spiral arm and disk regions containing not more than one emitting knot in Hα or continuum constitute the first category, which contains 145 objects. Photometry is also performed using bigger apertures enclosing neighboring emission complexes. These form our second category and there are 26 such regions selected from the galaxies NGC 2366, 2997, and NGC 4303. Nuclear H II regions (hotspots) are grouped into third category (15 regions) and are in galaxies NGC 1365, 2903, and 3351. In this section we compare the observational properties for these three categories separately.

Histogram distribution of Hα+[N II] equivalent widths, $B-V$ and $V-R$ colors are shown in Figs. 12(a)-12(c). Contributions from the three categories are as denoted. Statistical properties are given separately in Table 4. Category 2 region colors and equivalent widths are similar to that of category 1, with increased contributions in V and Hα+[N II] bands, which can be easily explained as due to the contributions from multiple regions. Thus colors are not much affected by increased aperture sizes ($B-V$: 0.30 vs 0.21, $V-R$: 0.44 vs 0.48), while equivalent widths marginally decrease (167 vs 213). The observed differences in $B-V$ and $V-R$ colors is most likely due to under subtracted background, which implies that the H II regions are bluer in $B-V$ and redder in $V-R$ compared to background. In contrast hotspots are redder ($B-V$: 0.58 vs 0.21, $V-R$: 0.58 vs 0.48), brighter in both V (14.95 vs 17.76) and Hα+[N II] (−12.74 vs −13.31) and have lower Hα+[N II] equivalent widths (40 vs 213). Segregation of hotspots into regions of redder colors and lower equivalent widths is clearly seen in the histograms. The regions for background measurements are chosen just outside the hotspots and hence are not the causes of red colors and lower emission equivalent widths. As noted in the introduction [N II] may not contribute more than 30% to Hα +[N II] flux. The observed difference in equivalent widths between disk and nuclear regions are hence due to Hα equivalent width differences rather than [N II] differences. Kennicutt *et al.* (1989) had earlier reported lower equivalent widths for nuclear H II regions, which is consistent with our results. While colors can be reddened due to higher reddening in the nuclear regions, equivalent widths are unaffected by reddening. On the other hand lower equivalent widths and higher continuum fluxes might be a result of extended dura-

tion of star formation. Thus hotspots are distinct from GEHRs in history and cannot be just scaled up versions of GEHRs.

There are 42 (29%) GEHRs with Hα+[N II] equivalent widths exceeding 300 Å with 25 (17%) of them having equivalent widths greater than 350 Å, all of which are in disks and spiral arms of program galaxies. High equivalent widths imply that these regions are extremely young. *R* magnitudes and Hα+[N II] fluxes of GEHRs are plotted against the Hα+[N II] equivalent widths in Fig. 13. The high equivalent width regions are not necessarily the ones with the highest Hα+[N II] fluxes. There are many high equivalent width regions with less than average continuum, with normal or less than average Hα+[N II]. In other words, a significant fraction of the youngest regions lie at the fainter limit in both *R* and Hα and hence were less favoured in spectroscopic

TABLE 3. Photometric catalogue of H II regions.*

Id	X	Y	RA	DEC	DIA	V	$B-V$	$V-R$	log $F\alpha$	W(Hα)	Qual.	Other Id
1	2	3	4	5	6	7	8	9	10	11	12	13
						NGC1365						
1	365	346	W047	N115	8.6	16.75	0.18	0.16	−12.90	245	1	RW-B
2	337	351	W049	N105	15.0	15.77	0.17	0.30	−12.47	236	1	RW-C,L7
3	296	390	W062	N090	9.3	16.95	0.25	0.24	−12.95	246	1	RW-D,L15
4	266	377	W058	N080	11.4	16.32	0.25	0.23	−12.91	148	1	RW-E
5	234	397	W065	N068	12.9	16.24	0.34	0.18	−13.20	76	1	RW-F
6	203	429	W076	N057	12.9	16.22	0.28	0.20	−13.03	107	1	RW-F
7	144	441	W081	N036	7.9	18.47	0.25	0.44	−13.33	338	4	
8	111	452	W085	N024	12.1	16.93	0.24	0.34	−12.82	293	3	L28
9	325	285	W025	N101	10.7	17.36	0.16	0.28	−12.70	607	3	
10	343	252	W013	N107	10.0	17.30	0.27	0.24	−12.95	334	1	
11	65	479	W094	N008	7.1	17.58	0.10	0.61	−12.90	345	3	L6
12	15	472	W092	S010	7.1	17.31	0.41	0.49	−13.06	208	1	
13	89	168	E017	N017	8.6	16.18	0.31	0.63	−12.43	279	2	L4
14	73	211	E001	N011	8.6	14.84	0.57	0.52	−12.39	98	1	L12
15	30	234	W007	S005	7.9	14.21	0.59	0.58	−12.21	78	1	L3
16	43	215	W000	S000	5.0	15.01	1.51	1.05	−12.35	77	1	Nuc
						NGC1566						
1	341	294	W016	N074	5.0	> 18.00	–	–	−12.98	>322	4	RW-A
2	324	304	W019	N068	9.3	15.94	−0.11	0.74	−12.12	403	4	RW-B,HP-I
3	305	310	W021	N061	7.9	16.17	0.12	0.59	−12.47	260	3	RW-C,HP-II
4	210	367	W042	N028	11.4	15.87	0.20	0.38	−12.80	112	4	RW-D,HP-IV
5	136	369	W042	N001	14.3	15.62	0.16	0.55	−12.25	265	4	RW-E,HP-VI
6	72	210	E014	S022	6.4	18.16	0.61	0.71	−13.18	284	4	
7	94	193	E020	S014	9.3	17.53	−0.24	0.38	−14.04	30	4	
8	111	181	E025	S008	6.4	18.02	0.15	0.73	−14.22	22	2	
9	204	274	W008	N025	10.7	17.05	0.82	0.53	−13.52	55	4	
10	219	248	E001	N031	10.0	17.38	0.41	0.41	−13.16	187	4	
11	105	126	E044	S010	17.9	15.74	−0.20	0.44	−12.73	110	4	HP-V
12	53	127	E044	S029	14.3	16.05	−0.01	0.53	−12.58	188	2	HP-III
						NGC2366						
1	102	278	–	–	25.0	13.76	0.14	0.39	−11.24	577	1	NGC2363
2	122	228	–	–	19.8	15.60	−0.03	0.70	−12.23	242	1	HK54
3	108	263	–	–	53.6	13.52	0.11	0.60	−11.16	458	1	1+2
						NGC2903						
1	125	370	W011	S078	8.6	17.30	0.39	0.88	−12.68	342	2	M−003−070
2	114	231	E039	S082	11.4	16.71	0.03	0.56	−12.66	283	2	M+047−072
3	96	255	E030	S088	6.4	>18.00	–	–	−12.98	>450	4	M+039−078
4	152	305	E012	S068	8.6	>18.00	–	–	−12.86	>600	4	
5	126	404	W023	S077	7.1	16.99	0.38	0.54	−13.04	156	1	
6	315	358	W006	S010	6.4	15.27	0.48	0.44	−14.68	−1	1	Oka-e
7	327	342	W001	S006	5.0	14.82	0.51	0.54	−12.88	30	1	Oka-c
8	335	348	W003	S003	3.6	15.90	0.75	0.74	−13.25	29	1	Tpp-n
9	347	349	W003	N001	5.7	14.95	0.58	0.64	−12.42	89	1	Oka-d
10	359	337	E001	N006	6.4	14.70	0.42	0.49	−12.74	40	1	Oka-a
11	343	340	E000	N000	5.0	15.10	0.65	0.69	−12.51	81	1	Oka-b

TABLE 3. (continued)

Id	X	Y	RA	DEC	DIA	V	$B-V$	$V-R$	log $F\alpha$	W(Hα)	Qual.	Other Id
1	2	3	4	5	6	7	8	9	10	11	12	13
12	441	274	E023	N035	6.4	17.72	−0.20	0.62	−12.87	417	4	M+024+047
13	516	349	W004	N061	9.3	16.71	0.17	0.79	−12.48	339	2	M−003+069
14	621	394	W020	N099	7.1	>19.00	–	–	−13.52	>700	4	M−021+105
15	593	392	W019	N089	7.1	17.99	0.08	0.41	−13.31	233	4	
16	484	384	W016	N050	8.6	18.19	0.11	0.84	−12.99	393	4	
17	542	123	E077	N071	7.9	18.16	0.12	0.49	−13.31	255	4	
18	506	246	E033	N058	5.7	17.25	0.09	0.49	−13.38	95	2	
						NGC 2997-NE						
1	268	123	E080	N059	6.4	17.49	0.28	0.81	−12.79	340	2	RW-B
2	255	133	E076	N055	5.0	18.07	0.23	0.40	−13.27	284	2	RW-C
3	267	162	E066	N059	7.1	>19.00	–	–	−13.23	>400	4	RW-D
4	277	186	E057	N062	5.0	>19.00	–	–	−13.57	>400	4	RW-E,WR13
5	290	214	E047	N067	5.7	>19.00	–	–	−13.62	>250	4	RW-F
6	296	237	E039	N069	10.7	>19.00	–	–	−13.60	>350	4	RW-G
7	294	249	E035	N069	4.3	18.74	0.13	0.35	−13.71	196	3	RW-G
8	287	261	E030	N066	5.0	18.75	0.02	0.24	−13.71	220	4	
9	299	275	E025	N070	7.1	19.10	0.11	0.52	−13.66	263	4	RW-H
10	302	293	E019	N071	7.9	17.45	0.08	0.31	−13.27	175	3	RW-I,WR20
11	303	314	E011	N072	6.4	>19.00	–	–	−13.35	>350	4	RW-J
12	295	330	E006	N069	5.0	18.47	0.20	0.44	−13.47	247	3	RW-K
13	310	352	W002	N074	4.3	18.88	0.09	0.24	−13.82	192	4	RW-L,WR23
14	304	360	W005	N072	3.6	19.13	0.19	0.36	−14.19	93	3	
15	304	373	W010	N072	5.0	>19.00	–	–	−13.56	>350	4	
16	279	410	W023	N063	7.9	18.93	0.93	0.62	−13.47	320	4	
17	260	427	W029	N056	6.4	18.29	0.53	0.39	−13.66	143	4	
18	202	497	W054	N036	5.7	>19.00	–	–	−13.62	>300	4	
19	150	492	W052	N017	5.7	>19.00	–	–	−13.91	>350	4	
20	98	501	W055	S001	9.3	18.54	−0.16	0.74	−13.51	181	4	
21	332	521	W062	N082	3.6	>19.00	–	–	−13.87	>400	4	
22	332	532	W066	N082	3.6	18.80	0.33	−0.10	−14.49	53	4	
23	292	442	W034	N068	5.7	>19.00	–	–	−13.50	>350	4	
24	362	342	E001	N093	10.0	18.17	0.16	0.25	−13.70	132	4	
25	352	242	E037	N089	8.6	19.17	0.24	0.75	−13.71	203	4	
26	261	300	E016	N057	7.9	>19.00	–	–	−13.59	>550	4	
27	203	282	E023	N036	3.6	19.03	0.18	0.01	−14.51	>50	4	
28	214	285	E022	N040	3.6	18.74	0.13	−0.01	−14.34	>50	4	
29	322	174	E061	N079	4.3	>19.00	–	–	−13.95	>250	4	
30	304	142	E073	N072	6.4	18.11	0.36	0.36	−13.65	125	4	
31	298	125	E079	N070	5.7	18.67	0.41	0.57	−13.41	>300	4	
32	279	111	E084	N063	7.1	18.13	0.29	0.32	−13.68	124	4	
33	247	56	E104	N052	7.1	>19.00	–	–	−13.55	>300	2	
34	163	48	E106	N022	4.3	17.65	0.32	0.54	−13.40	122	4	
35	172	77	E096	N025	6.4	>19.00	–	–	−13.94	>150	4	
36	212	134	E076	N039	5.7	>19.00	–	–	−14.03	>700	2	
						NGC 2997-NE (Groups)						
1	269	124	E079	N060	17.9	15.72	0.38	0.53	−12.29	273	2	1+2+32
2	294	250	E034	N069	14.3	16.97	0.07	0.56	−12.94	188	4	6+7+8
3	294	277	E025	N069	8.6	18.05	0.20	0.46	−13.34	226	4	9
4	300	324	E008	N071	12.9	17.52	0.18	0.77	−12.82	336	4	10+11+12
5	303	362	W006	N072	14.3	17.70	0.30	0.49	−12.97	363	4	13+14+15
6	337	525	W064	N084	10.7	18.14	0.14	0.11	−13.41	288	4	21+22
7	209	284	E022	N038	18.6	16.96	0.03	0.30	−13.09	168	4	27+28
8	168	49	E106	N024	14.3	16.49	0.19	0.61	−13.01	98	4	34+35
9	300	133	E076	N071	12.9	16.80	0.37	0.44	−12.94	177	4	30+31
						NGC 2997-SW						
1	145	55	E042	S065	9.3	17.25	0.54	0.61	−13.17	137	3	WR15
2	128	204	W011	S071	8.6	17.28	0.40	0.73	−12.76	335	3	WR24
3	148	366	W069	S064	13.6	16.35	0.33	0.52	−12.87	132	2	WR31
4	270	437	W095	S020	9.3	17.45	−0.06	0.47	−13.27	149	4	WR33
5	246	490	W113	S029	7.1	19.10	0.25	0.84	−14.12	70	4	WR37
6	320	460	W103	S002	7.1	18.78	0.14	0.60	−13.53	253	4	

TABLE 3. (continued)

Id	X	Y	RA	DEC	DIA	V	$B-V$	$V-R$	log $F\alpha$	W(Hα)	Qual.	Other Id
1	2	3	4	5	6	7	8	9	10	11	12	13
7	230	432	W093	S035	9.3	17.55	0.39	0.52	−13.19	190	4	
8	187	459	W103	S050	7.9	17.84	0.22	0.41	−13.43	157	4	
9	180	417	W087	S053	8.6	17.39	0.18	0.42	−13.29	142	2	
10	101	443	W097	S081	5.0	17.86	0.31	0.33	−14.04	42	1	
11	166	354	W065	S058	6.4	18.52	0.20	0.66	−13.52	192	4	
12	151	302	W046	S063	17.9	16.04	0.23	0.41	−13.26	45	3	
13	157	265	W033	S061	8.6	18.50	0.84	0.50	−13.36	313	4	
14	159	236	W023	S060	5.0	19.12	0.13	1.06	−13.30	392	4	
15	155	214	W015	S061	6.4	17.77	0.38	0.55	−13.45	124	1	
							NGC 3351					
1	337	235	E023	N066	7.1	17.59	−0.04	0.38	−13.53	101	4	M+014−067
2	134	302	W001	S006	6.4	14.61	0.55	0.60	−12.57	48	1	M−004−006
3	137	288	E004	S005	4.3	15.54	0.55	0.50	−13.48	15	1	AN-a3
4	152	282	E006	N000	7.1	14.45	0.45	0.47	−12.73	32	1	AN-a1
5	166	295	E001	N005	5.0	15.42	0.69	0.61	−12.81	58	1	AN-c1
6	159	307	W003	N003	5.7	14.39	0.63	0.51	−12.86	22	1	AN-d
7	151	299	E000	N000	3.6	15.42	0.94	0.67	−14.71	1	1	AN-e(Nuc)
							NGC 4303					
1	57	348	W030	S039	4.3	18.44	0.34	0.69	−13.32	264	2	
2	56	360	W034	S039	4.3	17.86	0.06	0.40	−13.51	133	2	
3	46	334	W025	S043	7.1	16.96	0.25	0.44	−12.88	240	2	HK175
4	47	309	W016	S042	9.3	15.90	0.21	0.48	−12.42	249	1	HK155
5	47	243	E007	S042	6.4	17.60	0.63	0.53	−13.25	170	2	
6	71	206	E021	S034	6.4	17.26	0.30	0.48	−13.01	223	2	
7	52	183	E029	S041	7.1	17.64	0.45	0.64	−13.11	217	4	HK76
8	98	144	E043	S024	10.7	16.66	0.04	0.51	−13.22	77	2	
9	180	138	E045	N005	8.6	16.48	0.25	0.45	−12.88	153	1	HK49
10	206	98	E059	N014	7.9	17.62	0.68	0.60	−13.32	136	4	
11	183	88	E063	N006	8.6	17.03	0.09	0.12	−14.80	<20	2	
12	230	50	E076	N023	6.4	18.35	0.07	0.67	−13.33	246	4	
13	259	255	E003	N033	4.3	18.52	0.03	0.50	−13.70	143	4	
14	241	320	W020	N027	4.3	19.35	0.50	0.87	−13.64	253	4	
15	279	294	W011	N040	5.0	18.85	0.02	0.64	−13.69	173	4	
16	281	313	W017	N041	5.0	18.21	0.16	0.25	−13.84	98	2	
17	263	305	W015	N035	8.6	17.55	0.42	0.48	−13.78	49	2	
18	257	321	W020	N032	4.3	18.65	0.53	0.20	−14.30	54	3	
19	304	299	W012	N049	5.0	18.39	1.18	0.73	−13.28	272	3	HK157
20	320	292	W010	N055	5.7	17.64	0.63	0.41	−13.42	131	2	
21	294	263	E000	N046	5.7	18.49	0.16	0.85	−13.22	302	4	HK135
22	312	211	E019	N052	6.4	18.18	0.34	1.04	−13.00	315	4	
23	328	209	E020	N058	6.4	16.99	0.34	0.33	−13.38	85	2	
24	351	193	E025	N066	6.4	16.48	0.20	0.35	−12.97	136	1	HK91
25	353	168	E034	N067	5.0	18.98	0.17	0.91	−13.38	312	4	
26	333	181	E030	N060	8.6	16.19	0.14	0.30	−13.20	64	1	
27	143	205	E021	S008	6.4	19.07	0.60	0.59	−13.49	352	4	HK95
28	222	344	W029	N020	7.9	>19.00	–	–	−13.84	235	4	
29	314	272	W003	N053	5.7	16.79	0.49	0.38	−13.46	57	1	
30	285	220	E016	N042	7.9	17.15	0.39	0.41	−13.46	77	1	
31	359	139	E045	N069	9.3	18.03	0.45	0.66	−13.63	92	4	
32	296	141	E044	N046	7.9	>19.00	–	–	−13.45	>900	4	
33	294	160	E037	N046	5.0	>19.00	–	–	−13.44	>1300	4	
34	282	128	E049	N041	5.7	>19.00	–	–	−13.53	>700	4	
35	211	158	E038	N016	8.6	17.02	0.38	0.45	−13.18	124	2	
36	139	140	E044	S010	5.7	18.29	0.68	0.50	−13.66	127	4	
37	92	168	E034	S026	8.6	17.92	0.46	0.26	−13.63	122	4	
38	48	284	W007	S042	7.9	17.21	0.77	0.50	−13.31	108	2	
39	75	396	W047	S032	5.7	17.76	0.50	0.37	−13.98	43	1	
40	101	382	W042	S023	7.1	18.45	0.20	0.61	−13.28	317	4	

TABLE 3. (continued)

Id	X	Y	RA	DEC	DIA	V	$B-V$	$V-R$	log $F\alpha$	W(Hα)	Qual.	Other Id
1	2	3	4	5	6	7	8	9	10	11	12	13
						NGC 4303 (Groups)						
1	237	475	W075	N025	28.6	15.19	0.63	0.12	−12.44	173	4	
2	154	403	W050	S004	21.4	16.16	0.31	0.23	−13.07	90	4	39+40
3	50	349	W030	S041	16.4	16.68	−0.36	0.44	−12.41	539	4	1+2+3
4	45	293	W010	S043	17.9	15.37	0.35	0.49	−12.38	166	2	4+38
5	62	256	E003	S037	9.3	16.29	0.60	0.27	−13.68	24	1	5
6	38	241	E008	S046	10.7	17.25	0.35	0.50	−12.95	248	4	
7	91	145	E042	S027	9.3	16.86	−0.03	0.61	−13.17	95	2	8
8	137	128	E049	S010	21.4	15.08	0.38	0.49	−12.82	46	2	36
9	180	136	E046	N005	8.6	16.49	0.24	0.46	−12.87	154	1	9
10	194	92	E061	N010	17.9	15.86	0.30	0.34	−12.81	110	3	10+11
11	210	154	E039	N016	10.7	16.74	0.42	0.43	−13.06	132	2	35
12	287	143	E043	N043	17.1	>19.00	–	–	−12.77	>1000	4	32+33+34
13	351	192	E026	N066	6.4	16.05	0.27	0.38	−12.85	118	1	24
14	334	183	E029	N060	6.4	16.14	0.36	0.25	−13.45	36	1	26
15	321	208	E020	N055	11.4	15.24	0.50	0.31	−12.78	69	1	22+23
16	313	295	W011	N052	12.1	15.80	0.38	0.44	−12.75	110	1	19+20
						NGC 4449						
1	273	55	E080	N047	16.4	15.58	0.26	0.51	−12.33	228	1	
2	311	109	E061	N061	10.7	17.23	0.05	0.66	−12.59	507	1	
3	231	205	E026	N032	15.7	15.10	0.07	0.29	−12.71	74	1	
4	159	210	E025	N006	11.4	15.39	0.11	0.45	−12.53	129	1	
5	160	244	E012	N007	15.0	14.44	0.20	0.40	−12.46	65	1	
6	190	253	E009	N017	10.0	14.98	0.12	0.33	−12.73	61	1	
7	109	230	E017	S011	15.7	15.40	0.23	0.53	−12.51	125	1	
8	41	230	E017	S036	15.0	15.65	0.19	0.55	−12.34	231	1	HK16
9	75	328	W017	S024	20.0	13.41	0.02	0.30	−11.79	130	1	HK27
10	298	250	E010	N056	20.0	14.88	0.12	0.32	−12.76	52	1	
11	342	274	E002	N072	15.7	16.02	0.03	0.46	−12.44	280	1	
12	140	278	E000	S000	12.1	13.59	0.22	0.38	−12.20	55	1	Nuc
						NGC 5253						
1	191	257	E000	S000	9.3	13.31	0.33	0.37	−11.24	383	1	Nuc
2	164	265	W003	S010	9.3	13.96	0.16	0.38	−11.84	175	1	HS

The notations used for Identification in the last column in TABLE 3 are :
CM : Crillon and Monnet (1969)
HK : Hodge and Kennicutt (1983)
HP : Hawley and Phillips (1980)
AN : Alloin and Nieto (1982)
Oka : Oka *et. al* (1974)
Tpp : Prabhu (1980)
L : Lindblad, P.O. (see Alloin *et. al* 1981)
M : McCall, Rybski, and Shields (1985)
RW : Roy and Walsh (1986, 1987, 1988)
WR : Walsh and Roy (1989a,b)

*Table 3 is presented in its complete form in the ApJ/AJ CD-ROM Series, Volume 3, 1994.

observations. This explains the absence of high equivalent width regions in flux limited samples mostly observed spectroscopically. Viallefond (1985, 1987) had earlier noticed the lack of high equivalent width regions in a compilation of spectroscopic data on H II regions and H II galaxies, and discussed several scenarios to explain the absence. Existence of significant number of such regions in our sample answers many of the questions raised by Viallefond, although it remains to be answered why the regions are not the brightest in Hα. It would be interesting to find out whether these regions are intrinsically fainter or dust obcuration is more towards these regions. These issues will be discussed in more detail in Paper III, while comparing the photometric results with evolutionary population synthesis models.

6. SUMMARY

Photometry in *BVR* continuum bands and in the emission line of Hα+[N II] are presented for a sample of H II complexes in disk, spiral arm and nuclear regions of galaxies NGC 1365, 1566, 2366, 2903, 2997, 3351, 4303, 4449, and 5253. The catalogued data form a comprehensive data base

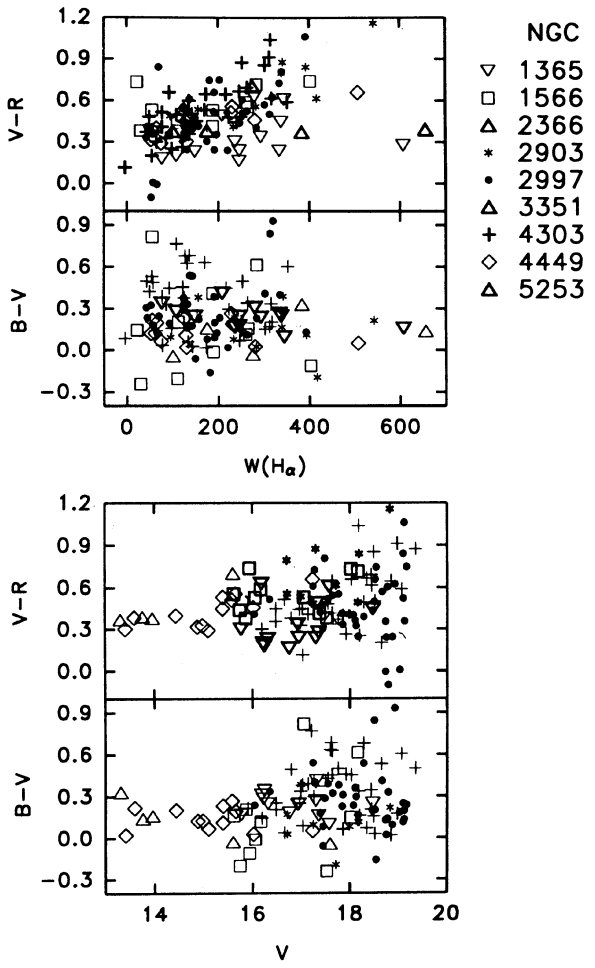

FIG. 9. Observed $B-V$ and $V-R$ colors of giant H II regions are plotted against the V magnitudes and Hα+[N II] equivalent widths. Regions from different galaxies are given different symbols. Absence of any systematic variation of colors with V magnitude suggests that there are no magnitude dependent systematic errors in our photometry. The larger spread in colors at fainter magnitudes is expected due to the background subtraction errors. $V-R$ color shows a trend with W(Hα), especially in NGC 2997 and 4303 due to the contamination from gaseous emission within R band.

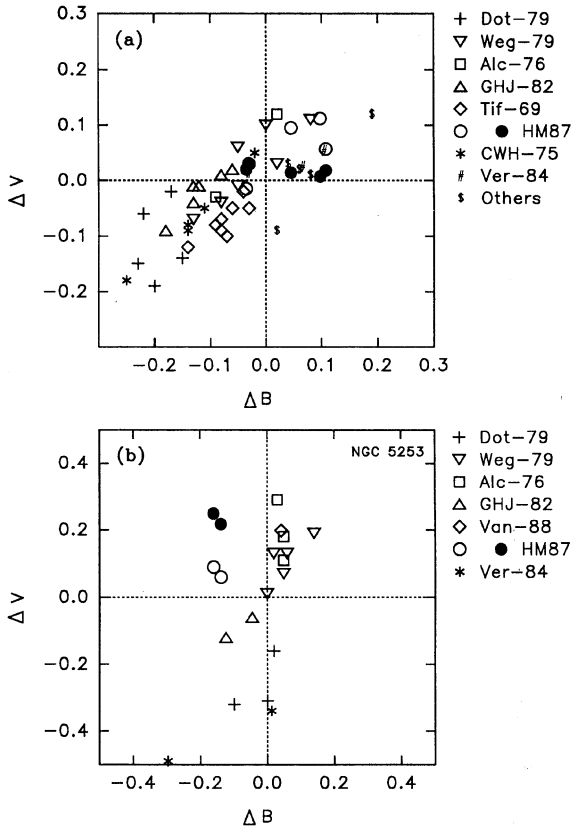

FIG. 10. Comparison of our BVR photometry around the nuclei of galaxies with those in the literature. V magnitude differences (ours–lit) are plotted against B and R (filled circle) magnitude differences for galaxies NGC 1365, 1566, 2903, 2997, 3351, 4303, and 4449 in (a) and for NGC 5253 in (b). Photometric measurements by different groups differ more for NGC 5253, especially in V band, which may be due to the emission rich spectrum of the nucleus. See text for details. The meaning of different author codes are as follows. Dot-79: Dottori (1979); Weg-79: Wegner (1979); Alc-76: Alcaino (1976); GHJ-82: Griersmith *et al.* (1982); Tif-69: Tifft (1961, 1969); HM-87: Hamuy & Maza (1987); CWH-75: Chincarini & Walker (1975); Ver-84: Veron-Cetty (1984); Van-88: Van den Bergh (1988); Others: Vorontsov-Velyaminov *et al.* (1973); Zasov & Lyuti (1973).

for the study of star formation in GEHRs. The photometric properties of giant H II regions are compared with nuclear H II regions. Colors and Hα+[N II] equivalent widths of nuclear H II regions are found to be distinctly different from disk H II regions, suggesting different star formation histories. 17% of the catalogued GEHRs have Hα+[N II] equivalent widths greater than 350 Å in contrast to a few regions identified spectroscopically. High equivalent width regions not necessarily being the brightest in the program galaxies pose interesting questions regarding the possible nature of the youngest star forming regions.

Dr. T. P. Prabhu encouraged this work and provided valuable suggestions for improving the manuscript. This research has made use of the NASA/IPAC Extragalactic Database (NED) which is operated by the Jet Propulsion Laboratory, California Institute of Technology, under contract with the National Aeronautics and Space Administration.

APPENDIX: ERROR ESTIMATION IN H II REGION PHOTOMETRY

1. Introduction

In recent years, digital photometry with CCDs is being extensively preferred over other methods of photometry. Development in software techniques has played a major role in this regard. Thus we have sophisticated stellar photometry routines in every software package that exists today. One of the areas where there is still a lot of scope for improvement is in the photometry of diffuse emitting regions superposed on a nonuniform background such as extragalactic H II complexes. H II complexes in nearby galaxies have angular sizes of several arcsec and hence are resolved by optical telescopes. Their structure differs from region to region and hence methods based on the uniformity of profiles cannot be used. Aperture photometry enclosing the full extent of the emitting surface with interactive choice of the regions, is one of the best ways of getting H II region fluxes. Recently Scowen (1991) described an "artificially intelligent" algorithm

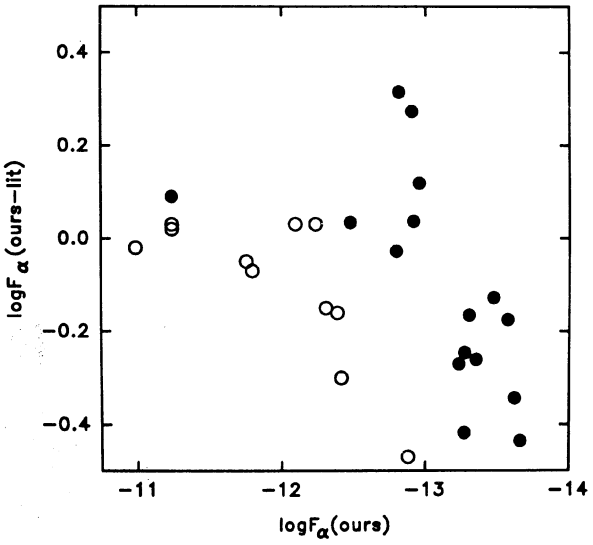

FIG. 11. Comparison of Hα photometry. Open circles are measurements through circular apertures by Kennicutt (1988) and Hunter (1982). The filled circles are from Roy and Walsh, who used rectangular apertures. Roy and Walsh fluxes are compared after dividing by the aperture areas.

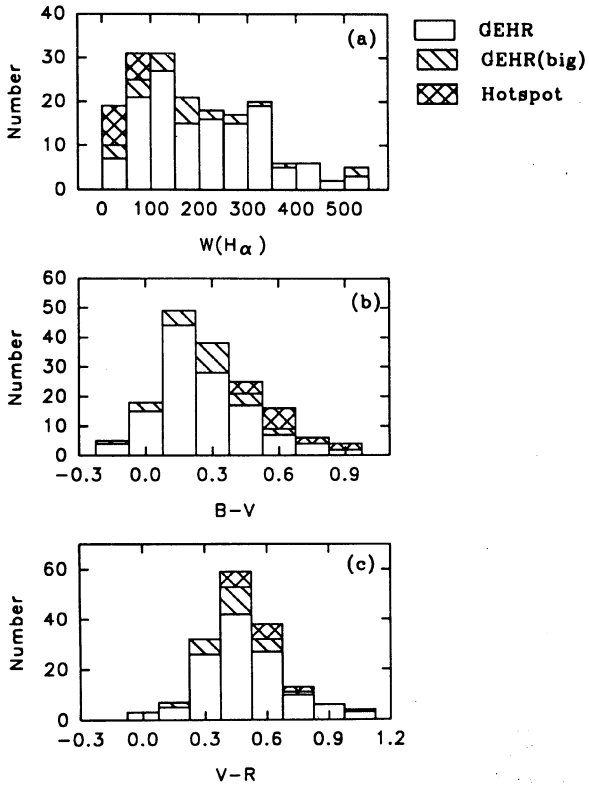

FIG. 12. Histograms of (a) $W(H\alpha+[N\,II])$, (b) $B-V$ and (c) $V-R$ colors for disk GEHRs, complexes of GEHRs and nuclear H II regions, respectively. Note that the nuclear H II regions have low $W(H\alpha)$, redder $B-V$ and $V-R$ colors.

to search out the spatial extent of regions above a predefined threshold and numerically register it. There are sources of errors intrinsic to H II region photometry, which affect both interactive and automatic methods of magnitude extraction.

One of the major errors in H II region photometry arises from improper subtraction of background values. It is necessary to have a model for the transparency of the underlying background before subtracting it. It is a good approximation to assume the H II regions to be fully transparent to disk/arm background light. The counts in the neighborhood of H II regions can be taken as the background value for that region. Selection of such regions for sky+background measurements is, however, nontrivial because small errors in the background estimation introduces large errors in photometry for the reasons listed below.

(1) Average surface brightness of H II regions is of the same order or less than the surface brightness of sky +background (see Table 2). With a typical sky+background value of $\mu_V=20.0$ and $\mu_R=19.0$ mag arcsec^{-2}, the expected V magnitude and flux within Hα band ($\Delta\lambda=160$ Å) using an aperture of 7 arcsec diameter is 16.04 mag and 2.80×10^{-13} erg s^{-1} cm^{-2}, respectively. Thus for H II regions fainter than the above limits, the background contribution is more than that of the H II region. The situation worsens if one uses bigger apertures. For regions fainter than 19 mag in V band and 3×10^{-14} erg s^{-1} cm^{-2} in Hα, the background contributes more than 90% to the total counts.

(2) Normally giant H II complexes are found in spiral arms where background is not only strong but also has a gradient. The counts in the outermost pixels around the H II regions are around 1.10–1.50 times that of the chosen value at the disk/arm interface. This makes the magnitudes very sensitive to the adopted regions for background estimates.

(3) Unlike in stellar photometry, background values cannot be estimated from an annular ring. This is because of possible faint extensions of H II complexes beyond the apertures chosen for measurements, and also due to the closeness of a neighbour.

It is necessary to keep the above facts in mind in performing H II region photometry. This requires software which can allow the users to select emission-free regions close to the emitting knots for background measurements. We have developed such a software which is briefly described below. The sensitivity of the derived fluxes on the estimated background is parametrized in terms of two parameters, namely (1) the fractional contribution of the assumed background relative to the total counts (y) and (2) true background counts expressed in units of the assumed background counts (x).

Circular apertures were used for flux measurements of H II regions with their aperture sizes decided so as to fully

TABLE 4. Median properties of GEHRs and hotspots.

H II Type	V	$B-V$	$V-R$	W(Hα)	log $F\alpha$	N
GEHRs	17.76	0.21	0.48	213	−13.31	145
GEHR groups†	16.49	0.30	0.44	167	−12.90	26
Hotspots	14.95	0.58	0.58	40	−12.74	15

† Measurements through bigger apertures containing neighbouring GEHRs.

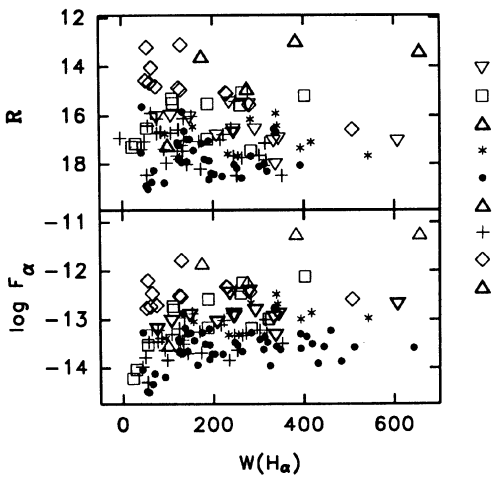

FIG. 13. R magnitude and Hα+[N II] flux is plotted against W(Hα+[N II]) for disk H II regions. The highest equivalent width regions (young regions) on an average are fainter both in Hα and R band.

enclose the emitting surface without encroaching neighbours. We selected pairs of rectangular regions flanking each of the H II regions in the direction perpendicular to the spiral arms interactively on the displayed image for the purposes of background estimation. Mostly the chosen background regions are in the disk/arm interface and hence the actual background values may be slightly higher than the one estimated ($x>1$). For some of the regions in the sample, sky dominates the sky+background counts. Interactive selection of regions is performed on COMTAL display unit and the programs were written under the STARLINK environment at the VAX 11/780 installation at Vainu Bappu Observatory.

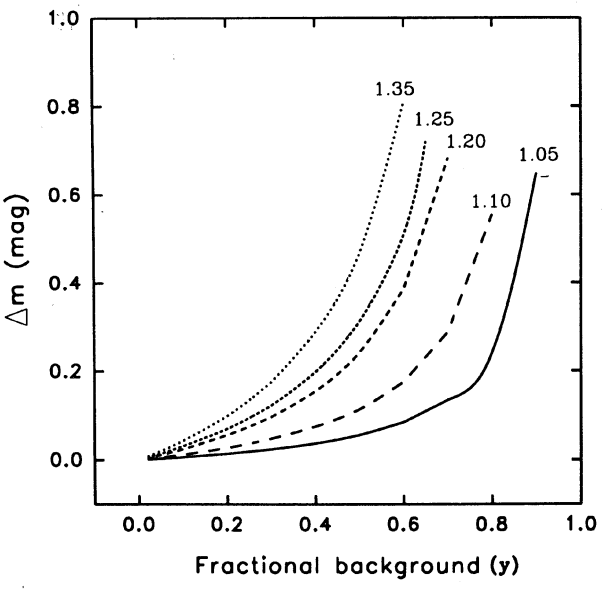

FIG. 14. Estimation of errors in the magnitude measurements of H II regions as a function of fractional background contribution (y), in the presence of a non-uniform background. x is the ratio of the actual background to the assumed background and is constant along a curve. For most of the H II regions x lies between 1.05–1.10 and y lies between 0.50–0.90.

2. Estimation of Errors due to Nonuniform Background

It was noticed often that growth curves continue to rise beyond the aperture used for magnitude extraction. This implies either that there is emission beyond the aperture size chosen or that the background is undersubtracted. In the former case, because the gas extends more than the stellar component, growth rate should be more in Hα compared to broadbands, which are continuum dominated. While this is true for some regions, there are many regions for which the growth rates in BVR bands match or even exceed the Hα growth rates. Thus faint extensions alone cannot be responsible for the observed growth rates. On the other hand increasing growth profiles may result from underestimation of the background. The growth profiles for Hα contain the continuum from the underlying background, which may be the reason for Hα growth rates. For some isolated regions we could flatten the growth profiles by choosing the regions for background measurements bit closer, resulting in around 10% increase over the estimated background values. Thus we believe the underestimated background values might be responsible for the increasing growth profiles. However it was not possible to choose background regions very close to all H II regions because of "crowding." At the same time, one can estimate the errors on the magnitudes for any chosen background on the assumption that true background is that which flattens the growth profiles. The approach we followed in estimating these errors is described below.

Magnitudes are defined as,

$$m_h = -2.5 \log(C_{h+b} - nC_b), \quad (1)$$

where C_b is the sky+background estimate per pixel in units of count s^{-1}, C_{h+b}, total count s^{-1} over n pixels enclosing the H II region and includes the background. Let $C_b = C_{b^-}$ be the background value used in the measurements, which normally shows increasing growth profile, and $C_b = C_{b^+}$ be the background value ("true") needed to flatten off the growth profiles.

$$m_{h^-} = -2.5 \log(C_{h+b} - nC_{b^+}), \quad (2)$$

$$m_{h^+} = -2.5 \log(C_{h+b} - nC_{b^-}). \quad (3)$$

m_{h^+} is the magnitude with the lower value of background (C_{b^-}) and hence an overestimate in brightness, while m_{h^-} is the magnitude with (C_{b^+}) as the background and hence close to the asymptotic value. The quantity $\Delta m = m_{h^-} - m_{h^+}$ is the amount by which the present measurements might be overestimated.

Let us define x and y as,

$$x = \frac{C_{b^+}}{C_{b^-}}, \quad y = \frac{nC_{b^-}}{C_{h+b}}. \quad (4)$$

Thus, by definition x is greater than or equal to 1, where as y is the fraction of the assumed background within the aperture and hence is always less than 1.

Substituting the values of x and y we get,

$$m_{h^-} = -2.5 \log[C_{h+b}(1-xy)], \quad (5)$$

$$m_{h^+} = -2.5 \log[C_{h+b}(1-y)], \quad (6)$$

$$\Delta m = -2.5[\log(1-xy) - \log(1-y)]. \quad (7)$$

With the above parametrization, the error Δm on the computed magnitude can be estimated as a function of x and y alone as shown in Fig. 14. For nonuniform background, x cannot be determined accurately and hence the above equation is very useful in estimating the errors on the resulting magnitude. As expected the errors on the magnitudes are too sensitive to changes in x when the background fraction (y) is greater than 80%, in which case $\Delta m = 0.5$ for a 10% increase in x over that assumed. This corresponds roughly to $V = 17.5$ and $F_\alpha = 7\times10^{-14}$ erg s^{-1} cm^{-2}. However the errors on the colors can be reduced by measuring the background values at the same location for all the bands, as was done in the present measurements.

Although in the above derivation we have defined x to be greater than 1, the equation can be used even for $x<1$ (regions where the true background is less than the mean), in which case Δm will be negative (underestimate and hence magnitudes should be made brighter). In general x can be treated as the variations over the mean value when the background is non-uniform. Thus Eq. (7) can be used to estimate the errors on the magnitudes for any object which is situated in a nonuniform background.

REFERENCES

Alcaino, G. 1976, A&AS, 26, 261
Alloin, D., Edmunds, M. G., Lindblad, P. O., & Pagel, B. E. J. 1981, A&A, 101, 377
Alloin, D., & Nieto, J.-L. 1982, A&AS, 50, 491
Bessell, M. S. 1990, PASP, 102, 1181
Bhat, P. N., Singh, K. P., Prabhu, T. P., & Kembhavi, A. K. 1992, J. Astrophys. Astr. 13, 293
Bottinelli, L., Gougenheim, L., Paturel, G., & de Vaucouleurs, G. 1984, A&AS, 56, 381
Chincarini, G., & Walker, M. F. 1975 (unpublished, see Longo & de Vaucouleurs 1983)
Crillon, R., & Monnet, G. 1969, A&A, 1, 449
de Vaucouleurs, G. 1979, AJ, 84, 1270
de Vaucouleurs, G., de Vaucouleurs, A., Corwin, H. G. 1976, Second Reference Catalogue of Bright Galaxies (Texas)
Dinerstein, H. L. 1990, in The Interstellar Medium in External Galaxies, edited by H. A. Thronson and J. M. Shull (Kluwer, Dordrecht), p. 257
Dottori, H. A. 1979, A&AS, 37, 519
Drissen, L., Moffat, A. F. J., & Shara, M. M. 1993a, AJ, 105, 1400
Drissen, L., Roy, J.-R, & Moffat, A. F. J. 1993b, AJ, 106, 1460
Gallagher, J. S., Hunter, D. A., & Tutukov, A. V. 1984, ApJ, 284, 544
Griersmith, D., Hyland, A. R., & Jones, T. J. 1982, AJ, 87, 1106
Hamuy, M., & Maza, J. 1987, A&AS, 68, 383
Hamuy, M., & Maza, J. 1989, AJ, 97, 720
Hawley, S. A., & Phillips, M. M. 1980, AJ, 235, 783
Hippelein, H. H. 1986, A&A, 160, 374
Hodge, P. W., & Kennicutt, R. C. 1983, AJ, 88, 296
Huchra, J. P. 1977, ApJ, 217, 928
Hunter, D. A. 1982, ApJ, 260, 81
Jones, J. E., & Jones, B. J. T. 1980, MNRAS, 191, 685
Kennicutt, R. C. 1981, ApJ, 247, 9
Kennicutt, R. C. 1983, ApJ, 272, 54
Kennicutt, R. C. 1984, ApJ, 287, 116
Kennicutt, R. C. 1988, ApJ, 334, 144
Kennicutt, R. C., Balick, B., & Heckman, T. 1980, PASP, 92, 134
Kennicutt, R. C., & Chu, Y. 1988, AJ, 95, 720
Kennicutt, R. C., Keel, W. C., & Blaha, C. A. 1989, AJ, 97, 1022
Kilkenny, D., & Menzies, J. W. 1989, South African Astron. Obs. Circ. 13, 25
Larson, R. B., & Tinsley, B. M. 1978, ApJ, 219, 46
Lequeux, J., Peimbert, M., Rayo, J. F., Serrano, A., & Torres-Peimbert, S. 1979, A&A, 80, 155
Longo, G., & de Vaucouleurs, A. 1983, Monographs in Astronomy, No. 3, Texas
Mayya, Y. D. 1991, J. Astrophys. Astr. 12, 319
Mayya, Y. D. 1993, Ph.D. thesis, Indian Institute of Science, Bangalore
McCall, M. L., Rybski, P. M., & Shields, G. A. 1985, ApJS, 57, 1
Melnick, J. 1977, ApJ, 213, 15
Newberry, M. V. 1991, PASP, 103, 122
O'Dell, C. R., & Castañeda, H. O. 1984a, ApJ, 283, 158
O'Dell, C. R., & Castañeda, H. O. 1984b, ApJ, 287, 116
Oka, S., Wakamatsu, K., Sakka, K., Nishida, M., & Jugaku, J. 1974, PASJ, 26, 289
Oke, J. B. 1974, ApJS, 27, 21
Parker, J. Wm., & Garmany, C. D. 1993, AJ, 106, 1471
Peimbert, M., Peña, M., & Torres-Peimbert, S. 1986, A&A, 158, 266
Pence, W. D., Taylor, K., & Atherton, P. 1990, ApJ, 357, 415
Peterson, C. J. 1978, ApJ, 226, 75
Prabhu, T. P. 1980, ApSpSci., 68, 519
Prabhu, T. P., Mayya, Y. D., & Anupama, G. C. 1992, J. Astrophys. Astr. 13, 129
Roy, J.-R., Arsenault, R., & Joncas, G. 1986, ApJ, 300, 624
Roy, J.-R., Walsh, J. R. 1986, MNRAS, 223, 39
Roy, J.-R., Walsh, J. R. 1987, MNRAS, 228, 883
Roy, J.-R., Walsh, J. R. 1988, MNRAS, 234, 977
Sandage, A. R., & Tammann, G. A. 1976, ApJ, 210, 7
Sandage, A. R., & Tammann. 1981, A Revised Shapley-Ames Catalog of Bright Galaxies (Carnegie Institution of Washington, Washington)
Scalo, J. M. 1986, Fund. of Cosmic Phys. 11, 1
Schild, H., & Testor, G. 1992, A&A, 266, 145
Schild, R. E. 1983, PASP, 95, 1021
Scowen, P. A. 1991, PASP, 103, 902
Sérsic, J. L., & Pastoriza, M. 1965, PASP, 77, 287
Shields, G. A. 1990, ARA&A, 28, 525
Shields, G. A., Skillman, E. D., & Kennicutt, R. C. 1991, ApJ, 371, 82
Tifft, W. G. 1961, AJ, 66, 390
Tifft, W. G. 1969, AJ, 74, 354
Van den Bergh, S. 1988, JRASC, 82, 13
Veron-Cetty M. P. 1984, A&AS, 58, 665
Viallefond, F. 1985, in Star-forming Dwarf Galaxies, edited by D. Kunth, T. X. Thuan, and J. T. T. Van (Editions Frontiere, Gif sur Yvette), p. 207
Viallefond, F. 1987, Ph.D. thesis, University of Paris
Vorontsov-Velyaminov, B. A., Lyuti, V. M., & Zaitseva, G. 1973, Sov. Astron. J. 16, 71
Waller, W. H. 1990, PASP, 102, 1217
Walsh, J. R., & Roy, J.-R. 1989a, MNRAS, 239, 297
Walsh, J. R., & Roy, J.-R. 1989b, ApJ, 341, 722
Wegner, G. 1979, ApSpSci, 60, 15
Zasov, A. V., & Lyuti, V. M. 1973, Sov. Astron. J. 17, 169